PHYSICAL REVIEW B **76**, 155127 (2007)

Enhanced thermoelectric performance of PbTe within the orthorhombic *Pnma* phase

Yi Wang, Xin Chen, Tian Cui, Yingli Niu, Yanchao Wang, Mei Wang, Yanming Ma,* and Guangtian Zou
National Laboratory of Superhard Materials, Jilin University, Changchun 130012, People's Republic of China

(Received 15 June 2007; revised manuscript received 10 September 2007; published 29 October 2007)

The thermoelectric properties of PbTe within the NaCl (B1) and the orthorhombic *Pnma* phases are extensively studied by *ab initio* calculations using the full-potential linearized augmented plane-wave method and the semiclassical Boltzmann theory. The calculations of *n*- and *p*-type Seebeck coefficients for the B1 structure suggested that the energy band gap plays an important role in determining the thermoelectric properties, but only at lower carrier concentrations. We found that the *n*-doped *Pnma* phase at 6.5 GPa has a larger Seebeck coefficient than that of the *n*-doped B1 phase at zero pressure, but has a comparable electric conductivity. This fact could be well understood by the large density of states in the conduction band and the large anisotropy in the band structure and constant energy surface. Our calculations also predicted that the largest *n*-type ZT values at 300 and 600 K of the *Pnma* phase at 6.5 GPa can reach up to 0.9 and 1.59, respectively, which are two times larger than those in B1 phase at zero pressure. The current theory strongly suggests that the *Pnma* structure of PbTe is an excellent thermoelectric material. It is desirable to synthesize the *Pnma* phase of PbTe at ambient pressure by making use of its high performance.

DOI: 10.1103/PhysRevB.76.155127 PACS number(s): 72.15.Jf, 71.20.Nr, 81.40.Rs

I. INTRODUCTION

The search for high-performance thermoelectric materials is a hot subject of current research. The performance of thermoelectric materials depends on the dimensionless figure of merit (ZT) given by $\mathrm{ZT}=S^2\sigma T/\kappa$, where S, σ, T, and κ are the Seebeck coefficient, electrical conductivity, absolute temperature, and thermal conductivity. High-performance of a thermoelectric material requires a high ZT with an effort to maximize the power factor $S^2\sigma$ and minimize κ. PbTe is one of the best thermoelectric materials used for thermoelectric generators for temperatures ranging between 400 and 800 K.[1] Previously, many attempts were made to improve its ZT value since the middle of the past century. Its alloys with SnTe and PbSe, and related compounds called TAGS (alloys of $\mathrm{AgSbTe_2}$ and GeTe), were for many years the best thermoelectric materials at temperatures ~700 K.[2] Moreover, PbTe doped with Ag and Sb became quaternary compounds $\mathrm{AgSbPb_{2n-2}Te_{2n}}$ (n=9 and 10), and the nanosized minority phase which is richer in Ag and Sb makes the PbTe matrix exhibit a high ZT of 2.2 at 800 K.[3,4] Recently, quantum wells of $\mathrm{PbTe/Pb_{1-x}Eu_xTe}$ and $\mathrm{PbSe_{0.98}Te_{0.02}/PbTe}$ superlattices[5,6] have also attracted considerable attention because their ZTs are all considered breakthrough in the decade-long ZT=1 barrier at room temperature.

PbTe is a narrow gap semiconductor (groups IV-VI), which crystallizes at ambient conditions in the NaCl (B1) phase.[7] Under high pressure, PbTe was found to transform to an intermediate phase at 6.0 GPa, and then to the CsCl phase at 13.0 GPa.[8,9] In 2005, the structure of the intermediate phase was solved by Rousse *et al.*[10] to be an orthorhombic *Pnma*. This structure corresponds to a distortion of the low-pressure B1 structure with a sevenfold coordination intermediate between the sixfold B1 and the eightfold CsCl (B2) structures.[10] Very recently, the experimental measurements suggest that high pressure could result in a significant enhancement of $S^2\sigma$ for PbTe-based thermoelectric materials,[11] particularly at the transition to the *Pnma* structure. However, up to now, the physical origin for the enhancement of thermoelectric efficiency in the *Pnma* phase remains unclear. In an effort to pursue a high ZT material, the understanding of the *Pnma* structure in PbTe is, thus, considered as essential. Also, it would be interesting to establish a direct link between its band structure and the thermoelectric properties. This *ab initio* approach not only rationalizes and predicts the optimal performance and doping level of the *p*- and *n*-type *Pnma* structures, but also predicts enhanced thermoelectric performances within the *Pnma* phase.

In this paper, we use the full-potential linearized augmented plane-wave (FP-LAPW) method based on density functional theory (DFT) to characterize the electronic structures, from which the thermoelectric properties were analyzed using the Boltzmann theory and the rigid band approach. Our calculations show that for *n*-type PbTe, the orthorhombic *Pnma* phase at 6.5 GPa has nearly two times larger ZT than that for the B1 phase at zero pressure. The high ZT in the *n*-type *Pnma* phases is mainly due to its large anisotropy in electronic structure and the large density of states (DOS) in the conduction band.

II. COMPUTATIONAL METHOD

The calculations were performed using the FP-LAPW method[12] within the DFT[13] through WIEN2K code.[14] The muffin tin radii were chosen to be 2.5 a.u. for both Pb and Te. The plane-wave cutoff was defined by $\min(R_{MT})\max(k_n)=10.0$, corresponding to approximately 391 and 6268 plane waves for the B1 and *Pnma* phases, respectively. We include the relativistic and spin-orbit coupling effects to account for Pb and Te due to their large atomic mass. An additional Pb $6p_{1/2}$ LO was added for a more accurate treatment of spin-orbit coupling. Convergence test gave the choices of 56 and 240 irreducible k points for the B1 and *Pnma* phases, respectively, in the electronic integration of the Brillouin zone (BZ). The transport properties were calculated using very large k point sets with 1240 and 1836 irreducible k

points. The exchange-correlation functional was described using both the Perdew-Burke-Ernzerhof[15] (PBE) and the Engel-Vosko[16] (EV) generalized gradient approximations (GGAs). The PBE-GGA[15] is the standard parameter-free GGA, while the EV-GGA has been designed by optimizing the exchange potential[16] rather than using E_{xc}. The reason for performing calculations using both GGAs is that a correct band gap is important for an accurate description of the thermoelectric properties. Standard GGA functionals are known to underestimate the band gap, and the EV-GGA has been shown in several cases to give band gaps in good agreement with experiment.[17]

The transport coefficients were calculated from the analysis of band structure calculations using the semiclassical Boltzmann theory[18] and the rigid band approach. This *ab initio* approach has been successful in rationalizing and predicting the optimal doping level of known compounds.[17,19–25] The rigid band approach to conductivity is based on the transport distribution

$$\sigma_{\alpha\beta}(\varepsilon) = \frac{1}{N}\sum_{i,\mathbf{k}} \sigma_{\alpha\beta}(i,\mathbf{k})\frac{\delta(\varepsilon-\varepsilon_{i,\mathbf{k}})}{d\varepsilon}, \qquad (1)$$

where N is the number of k points sampled. The k-dependent transport tensor is given as

$$\sigma_{\alpha\beta}(i,\mathbf{k}) = e^2\tau_{i,\mathbf{k}}v_\alpha(i,\mathbf{k})v_\beta(i,\mathbf{k}), \qquad (2)$$

and $\tau_{i,\mathbf{k}}$ is the relaxation time (it is also called the momentum relaxation time). The $v_\alpha(i,k)$ is a component of the group velocities

$$v_\alpha(i,\mathbf{k}) = \frac{1}{\hbar}\frac{\partial\varepsilon_{i,\mathbf{k}}}{\partial k_\alpha}. \qquad (3)$$

The transport coefficients as a function of temperature and chemical potential can be calculated by integrating the transport distribution

$$\sigma_{\alpha\beta}(T;\mu) = \frac{1}{\Omega}\int \sigma_{\alpha\beta}(\varepsilon)\left[-\frac{\partial f_\mu(T;\varepsilon)}{\partial\varepsilon}\right]d\varepsilon, \qquad (4)$$

$$\nu_{\alpha\beta}(T;\mu) = \frac{1}{eT\Omega}\int \sigma_{\alpha\beta}(\varepsilon)(\varepsilon-\mu)\left[-\frac{\partial f_\mu(T;\varepsilon)}{\partial\varepsilon}\right]d\varepsilon, \qquad (5)$$

where f is the Fermi-Dirac distribution function. The bands, and hence $\sigma(\varepsilon)$, are left fixed (thus "the rigid band approach"), and therefore, only one band structure information is needed per compound. The carrier concentrations can be represented by the chemical potential μ in Eqs. (4) and (5). Well, the conductivity can only be calculated with respect to the $\tau_{i,\mathbf{k}}$. The $\tau_{i,\mathbf{k}}$ should be included as a parameter; for simplicity and convenience, it is taken as direction independent[26] and a constant[27] in this work. So the Seebeck coefficient, $S=\sigma^{-1}\nu$, is then independent of $\tau_{i,\mathbf{k}}$ and can thus be calculated on an absolute scale.

In general, the relaxation time $\tau_{i,\mathbf{k}}$ in Eq. (2) comes from the ratio of the carrier energy $\varepsilon_{i,\mathbf{k}}$ (which is dependent on both the band index and the k vector direction) and the average energy of vibration of an atom, which is of the order of k_BT.[28] So choosing a constant for $\tau_{i,\mathbf{k}}$ in Eqs. (4) and (5) is an approximation for the real scattering mechanism and an average over the total relaxation time. There is a large departure in the value of Eqs. (4) and (5) between this approximation and real scattering if all the $\tau_{i,\mathbf{k}}$ are different significantly. So this approximation is only suitable for the carrier scattering which does not depend significantly on the wave vector (carrier energy[29]) and temperature, and this demands that the values of all $\tau_{i,\mathbf{k}}$ are approximately equal to each other. Although being a constant for $\tau_{i,\mathbf{k}}$ is an approximation to the real mechanisms of scattering, this approximation has been widely used in many cases[17,19,25,30,31] to calculate the transport coefficients successfully.

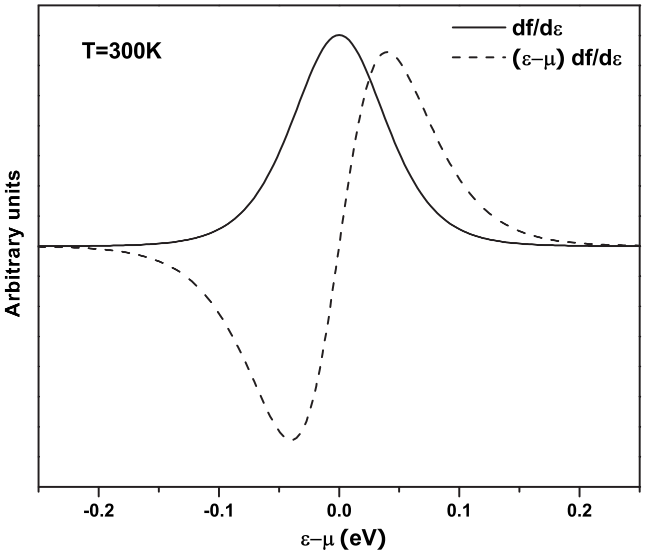

FIG. 1. Integrand factors $\partial f/\partial\varepsilon$ and $(\varepsilon-\mu)\partial f/\partial\varepsilon$ of PbTe within the *Pnma* phase at 6.5 GPa in Eqs. (4) and (5) at $T=300$ K.

Figure 1 shows the integrand factors of the *Pnma* phase in Eqs. (4) and (5) at $T=300$ K. It can be clearly seen that the distribution is quite broad and the transport coefficients are thus a sum over several Fermi surfaces. It is, therefore, very important that the energy band is correctly calculated.[27]

For the calculation of the transport tensors, the BOLTZTRAP code was used,[27] which is based on a well tested smoothed Fourier interpolation to obtain an analytical expression of the bands.[27] The original k mesh was interpolated onto a mesh five and ten times denser than the original for the B1 and *Pnma* structures, respectively.

It is important for thermoelectric materials to find an optimal ZT value, and one simple consideration can be made: thermal conductivity κ has both a lattice, κ_l, and an electronic, κ_e, component. κ_l is not available from the band structure calculations, but it is included as a constant in this work. The ratio between T and κ_e is, to a good approximation, given by the Wiedemann-Franz relation: $\kappa_e=L_0\sigma T$. Inserting the Lorentz number, $L_0=\pi^2/3(k_B/e)^2 = (156\ \mu\mathrm{V/K})^2$, ZT is seen to be expressed by the following:

$$\mathrm{ZT} = \frac{S^2\sigma T}{\kappa_e+\kappa_l} = \frac{S^2}{L_0+\kappa_l/(\sigma T)}. \qquad (6)$$

The *Seebeck coefficients* for PbTe at zero pressure and

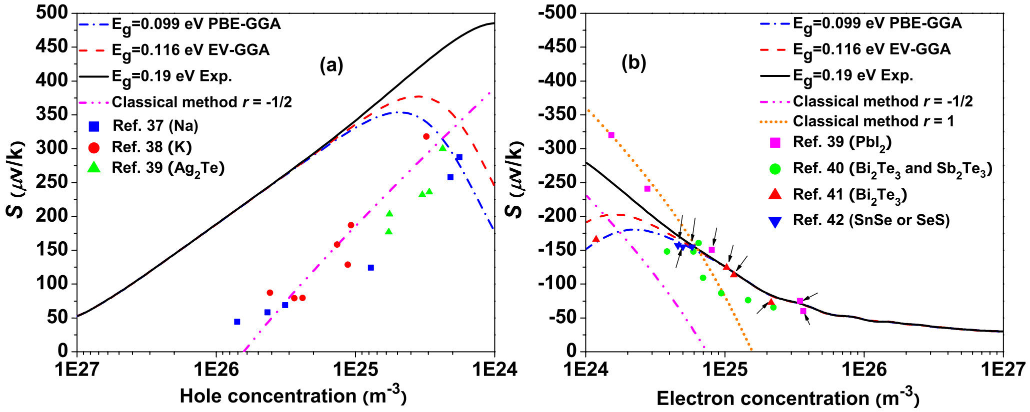

FIG. 2. (Color online) The calculated Seebeck coefficients for (a) p-type and (b) n-type PbTe within the B1 structure at zero pressure as a function of carrier concentration at 300 K. The dash-dot line, the dash line, and the solid line are the calculated results using energy gaps of 0.099, 0.116, and 0.19 eV, respectively. The experimental data (solid symbols) are also shown for comparison. The arrow marked experimental data in (b) are the selected experimental data to obtain the relaxation time τ. The dash-dot-dot line in (a) is the calculated Seebeck coefficients using the classical method with $r=-1/2$. The dash-dot-dot line and the short-dot line in (b) are the calculated Seebeck coefficients using the classical method with $r=-1/2$ and 1, respectively. The dopants in PbTe are shown in brackets.

300 K were also calculated using the "classical" approach[28] to compare with those obtained from the semiclassical Boltzmann method. Unlike the use of the constant relaxation time approximation in the Boltzmann method, this classical approach deals with the real mechanism of scattering[28] and adopts the average momentum relaxation time (which depends on all the momentum relaxation time, all the carrier energy, and temperature) to calculate the S. If the momentum relaxation time $\tau_{i,\mathrm{k}}$ obeys a power law

$$\tau_{i,\mathbf{k}} \propto \varepsilon_{i,\mathbf{k}}^{r}, \tag{7}$$

where the exponent r varies between $-1/2$ (for acoustic deformation potential scattering) and $+3/2$ (for ionized impurity scattering), the thermoelectric power of p- and n-type nondegenerate semiconductors (whose upper limit carrier concentration is in the order of magnitude of 10^{24} or 10^{25} carrier/m^3),[29] deduced from this classical method,[28] can be expressed as

$$S = (k_B/|e|)\left(r + \frac{5}{2} + \frac{\mu - \varepsilon_v}{k_B T}\right) \tag{8}$$

and

$$S = -(k_B/|e|)\left(r + \frac{5}{2} - \frac{\mu - \varepsilon_c}{k_B T}\right), \tag{9}$$

where k_B is the Boltzmann constant, $|e|$ is the elementary charge, $k_B/|e|$ is 86.16 μV/K, the ε_v is the valence band edge, and ε_c is the conduction band edge.

III. RESULTS AND DISCUSSION

A. Transport properties

The considerations of PBE-GGA and EV-GGA in the band structure calculation of the B1 phase at ambient pressure gave the band gaps of 0.099 and 0.116 eV, respectively, which are much smaller than the experimental value of 0.19 eV,[32,33] as expected. The underestimation of the band gap is a well-known problem of the Kohn-Sham theory.[34–36] Experience suggests that the shape of the band structure is correct and that most of the problem can be amended by a rigid shift of the conduction band. So we adopted the three different energy gaps to calculate S of the B1 phase at different carrier concentrations at 300 K, and the results are shown in Fig. 2 to compare with the experimental measurements.[37–42] It is found that for the n-doped system [Fig. 2(b)], the agreement between theory and experiments[39–42] is excellent within the carrier concentration ranging from 4×10^{24} to 4×10^{25} m^{-3}, without considering the kinds of dopants. Furthermore, by taking the experimental band gap of 0.19 eV, the measured data by Orihashi *et al.*[39] (the square dots), in which S shows a parabolic increased trend with decreasing carrier concentrations, can be well reproduced as shown in Fig. 2(b). Instead, with the smaller band gaps of 0.099 and 0.116 eV given by PBE-GGA and EV-GGA, the theoretical calculation deviates largely with the experimental data by Orihashi *et al.*,[39] at the carrier concentration region below 3×10^{24} m^{-3}. Note that the larger band gap by the EV-GGA gives better results than that by the PBE-GGA. For the p-doped system [Fig. 2(a)], the calculated S correctly reproduced the experimental trend, which shows a near linear increase with lowering concentration, but significantly overestimated the experimental value by about 200 μV/K. From the calculations for both n- and p-doped systems, it is obvious that the choice of band gap plays an important role in the calculation of S, but only at lower carrier concentration, while the effect is negligible at concentrations larger than 8×10^{24} and 2×10^{25} m^{-3} for n- and p-doped samples, respectively. Consequently, for a much reliable calculation, the experimental band gap of 0.19 eV was adopted for further calculation in the B1 structure. The arrow marked experimental values agree best with the calculated S, and then the experimental conductivity values of these dots are used to obtain the average relaxation time $\tau(4.48\times10^{-14}$ s) for all the $\tau_{i,\mathbf{k}}$ through the calculated σ/τ.

In order to find the physical origin of the large overestimation in the calculated S for p-type B1 PbTe shown in Fig. 2(a), we also employ the classical method[28] to calculate S at zero pressure and 300 K. For p-type B1 structure, it is previously[43] suggested that the lattice acoustic phonons dominate the carrier scattering at 300 K. Thus, the carrier scattering in the p-type B1 PbTe can be treated as the acoustic deformation potential scattering with a choice of $r=-1/2$.[28,43] It is remarkable that the p-type experimental S values are well reproduced in the whole range of carrier concentrations in this classical calculation with $r=-1/2$, as shown in Fig. 2(a). It is known that the classical method deals with the real mechanism of the carrier scattering.[28] Therefore, it is suggested that the constant relaxation time approximation, which cannot deal with the real scattering mechanism, is the main cause for the large overestimation of S in the semiclassical calculations for the p-type B1 structure [Fig. 2(a)]. However, for n-type PbTe at 300 K, the carrier scattering can only be described by complex combinations of the short-range potential of vacancies, the polar potential of the optical phonons, and the deformational potentials of optical and acoustic phonons.[44] While only the deformational potential of acoustic phonons obeys the power law in Eq. (7),[28] so it is difficult to find an appropriate r value in the classical calculation. Here, the calculations with a random choice of $r=-1/2$ result in a large deviation from the experimental values shown in Fig. 2(b). However, if we choose $r=1$, the experimental data can be well reproduced below the carrier concentration of 8×10^{24} m^{-1}, but an obvious discrepancy is evidenced at a higher concentration. It is noteworthy that the different optimal choices in r imply different scattering mechanisms for p- and n-type B1 PbTe. In view of the good agreement between the calculated results by the semiclassical method and the experimental data for n-type S in Fig. 2(b), it is suggested that the constant relaxation time approximation is appropriate to describe the carrier scattering in the n-type PbTe. Its scattering mechanism is thus not dependent significantly on the wave vector (electron energy) and temperature. For the *Pnma* phase of PbTe, due to the lack of information on the mechanism of carrier scattering, the classical calculation cannot be properly performed. Therefore, the semiclassical calculation is the last resort to rely on, which is the most often used in practice[17,19,25,27,30,31] to study the transport properties.

There is no clear band structure information reported in the literature for the high-pressure *Pnma* phase. The current calculations by PBE-GGA and EV-GGA give the indirect band gaps of 0 and 0.166 eV, respectively, at 6.5 GPa. Here, we choose the more reliable band gap of 0.166 eV calculated by EV-GGA to evaluate the S, σ/τ, and $S^2\sigma/\tau$ of the *Pnma* phase. The calculated results at 300 K are presented in Fig. 3. Transport coefficients of the B1 structure at zero pressure and 300 K are also shown for comparison. Compared to the B1 phase, the *Pnma* phase shows strong anisotropic behaviors in σ/τ, S, and $S^2\sigma/\tau$, especially for the σ/τ [Figs. 3(c) and 3(d)]. The orthorhombic symmetry of the *Pnma* structure means that the conductivity tensors will be diagonal and that $\sigma_{xx}\neq\sigma_{yy}\neq\sigma_{zz}$. As shown in Figs. 3(c) and 3(d), σ_{xx} is 15.4 times higher than σ_{zz} for the p-doped system, while the largest σ_{yy}/σ_{zz} is about 5.8 for the n-doped system. Note that the largest ratios of σ_{xx}/σ_{zz} and σ_{yy}/σ_{zz} are predicted to be 7.7 and 5.2 at a higher temperature of 600 K (not shown) for p- and n-type systems, respectively. Therefore, it is clear that the p-type sample has a larger anisotropy in the *Pnma* phase. Moreover, it is interesting to note that the anisotropy in the *Pnma* phase is larger than that of hexagonal Bi_2Te_3, where the ratio σ_{xx}/σ_{zz} is less than 5 at 300 K.[19] It should also be pointed out that the n-type *Pnma* phase has a larger S [Fig. 3(b)] and comparable σ/τ [Fig. 3(d)] along the y axis than those of the n-type B1 phase. Therefore, if we assume the same τ for the two phases, the resulting $S^2\sigma$ values along the y axis over all the carrier concentrations for the n-type *Pnma* phase at 6.5 GPa are found to be significantly larger than those for the B1 structure at 0 GPa [Fig. 3(f)]. This fact could be responsible for the experimentally observed enhancement of $S^2\sigma$.[11] However, for the p-type materials, the calculated maximum $S^2\sigma$ along the x axis in the *Pnma* phase at 6.5 GPa is smaller than that for the B1 structure [Fig. 3(e)] at zero pressure, resulting from its smaller S.

From Eq. (6), we calculate the ZT values for the B1 phase at zero pressure and the *Pnma* phase along its optimal crystal directions at 6.5 GPa. Here, we assume that τ and κ_l are independent of structures, doping level, and temperature. The choice of $\tau=4.48\times 10^{-14}$ s has been justified as described above. We chose κ_l values to be 2.15 and 1.0 W/mK, which are the lattice thermal conductivity of the undoped[39] and doped[42] B1 phases at zero pressure. The calculated ZT values with carrier concentrations for the B1 and *Pnma* phases at 300 and 600 K are shown in Fig. 4. Note that these results could guide future experiments in finding the optimal concentration of the doped samples. It can be clearly seen in Fig. 4(b) that the experimental ZT values for the n-type B1 phase at 300 K can be well reproduced by the calculated data, signifying the validity of the current model. On the contrary, because of the overestimated S for p-type B1 phase, the calculated ZTs do not agree well with the experimental data at 300 K in Fig. 4(a). It is noteworthy that the calculated ZTs of the n-type *Pnma* at 300 and 600 K are approximately two times larger than those of the n-type B1. Both desirable p- and n-type ZT values of the *Pnma* phase at 6.5 GPa reach up to 0.9 at 300 K, close to ZT≈1 (Refs. 45 and 46) of Bi_2Te_3, which is one of the best bulk thermoelectric materials at room temperature. Importantly, with temperature increasing up to 600 K, the largest ZT values of 2.18 (along the x axis) and 1.59 (along the y axis) for the p- and n-type materials have been predicted, signaling a kind of excellent thermoelectric material. However, one has to take caution for the large ZT values of the p-type material. As we have demonstrated in Fig. 2(a), the current semiclassical calculation overestimates the S for the p-type B1 by about 200 μV/K at 300 K, originated from the assumption of the constant relaxation time. So it is not straightforward to evaluate the exact performance of the p-type *Pnma* phase with the current calculation. Nevertheless, it is worth reminding that the p-type sample ($Pb_{0.393}Sn_{0.157}Te_{0.45}$) in the *Pnma* phase[11] has already been demonstrated as a good thermoelectric material. The experimental findings, thus, support our current predictions. It should be noted that the predicted ZT values for the n-type *Pnma* structure are suggested to be reliable by evidence of a satisfactory agreement with the experiments[11] and an accu-

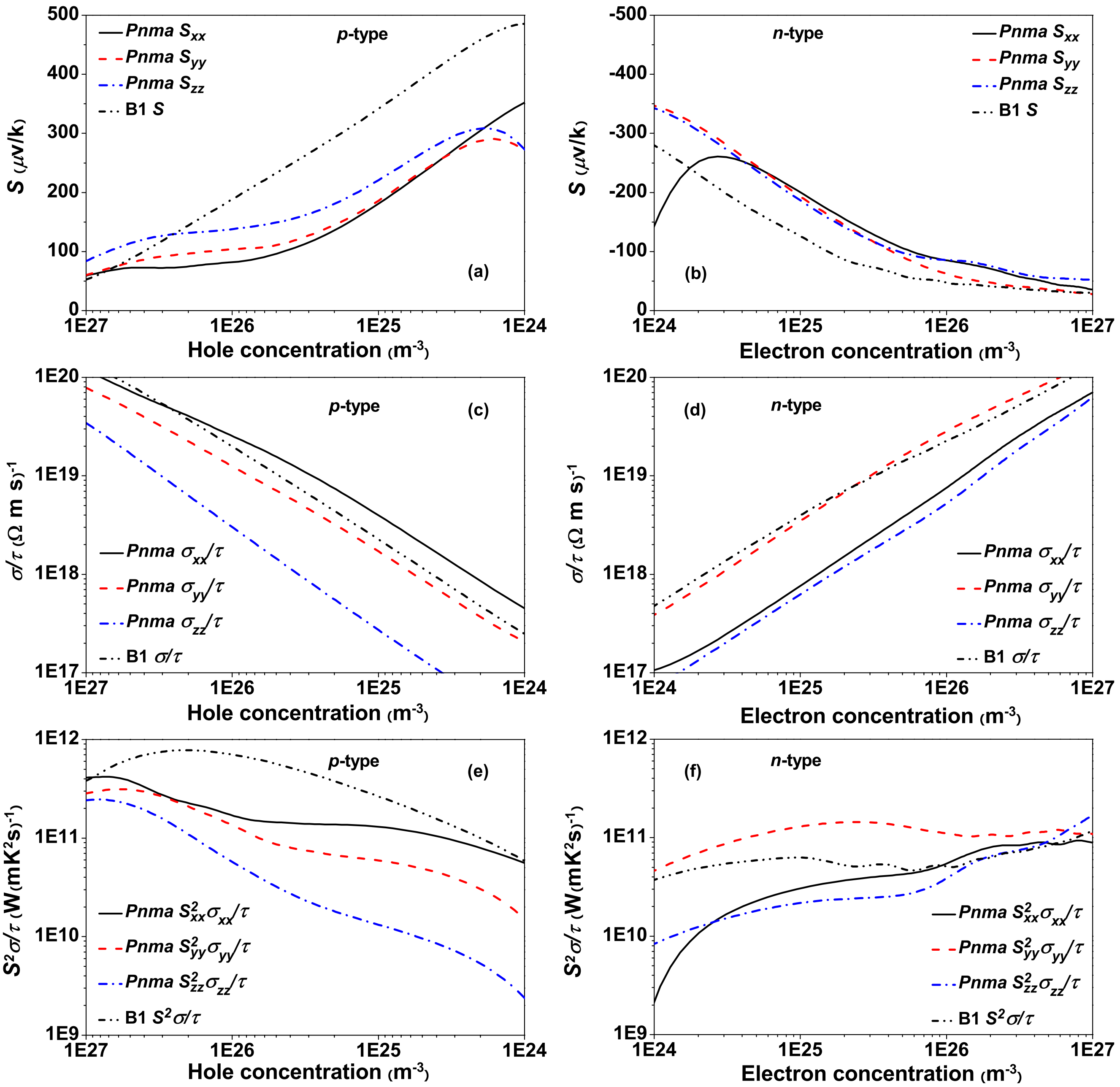

FIG. 3. (Color online) Transport properties of PbTe within the *Pnma* structure at 6.5 GPa and the B1 structure at zero pressure, as a function of carrier concentration at 300 K. (a) *p*-type Seebeck coefficients. (b) *n*-type Seebeck coefficients. (c) *p*-type electrical conductivities relative to relaxation time, σ/τ. (d) *n*-type electrical conductivities relative to relaxation time, σ/τ. (e) *p*-type power factors with respect to relaxation time, $S^2\sigma/\tau$. (f) *n*-type power factors with respect to relaxation time, $S^2\sigma/\tau$. The solid lines, the dash lines, and the dash-dot lines are the components of *xx*, *yy*, and *zz*, respectively, for the transport tensors of the *Pnma* phase. For the B1 phase, the components of *xx*, *yy*, and *zz* for the calculated tensors are equal, and the dash-dot-dot lines are one-third of the trace of the transport tensors.

rate description of the *n*-type B1 structure [Fig. 2(b)]. Our calculations also demonstrate that the optimal crystal direction of ZT in the *Pnma* phase is determined by the direction of optimal electric conductivity. These results are similar to the reports by Hicks and Dresselhaus.[47] They found that it is possible for an anisotropic crystal in three dimensions to increase ZT by choosing the current to flow along the direction of highest mobility. The strong anisotropy in the *Pnma* phase of PbTe at 6.5 GPa might be the main cause of its excellent thermoelectric properties.

B. Electronic structure

The total and partial electronic DOSs for the B1 and *Pnma* phases are presented in Fig. 5. For the sake of a clear comparison, we set the highest valence band (HVB) of the two phases as the zero energy level, and shift the lowest conduction band (LCB) to fix the band gap at 0.19 eV for the B1 phase and 0.166 eV for the *Pnma* phase. In the compounds, Pb 5*d* and Te 4*d* and 5*s* states are quite deep, and contribute little to the valence bands. From Figs. 5(b) and 5(c), it is clear that the valence bands are formed primarily

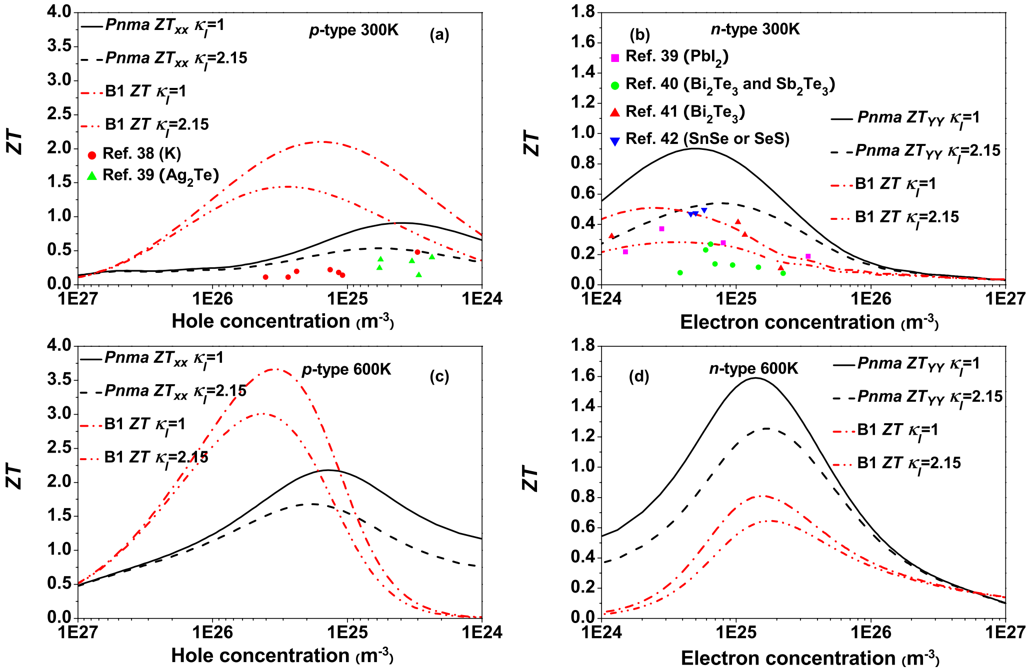

FIG. 4. (Color online) The calculated ZT values as a function of carrier concentrations at 300 and 600 K for PbTe within the B1 and *Pnma* structures at the pressures of 0 and 6.5 GPa, respectively. The solid lines and the dash lines are the ZT values along the optimal crystal directions of the *Pnma* structure calculated using $\kappa_l=1$ and $\kappa_l=2.15$ W/mK, respectively. The dash-dot lines and the dash-dot-dot lines are the ZT values of the B1 structure calculated from $\kappa_l=1$ and $\kappa_l=2.15$ W/mK, respectively. The experimental data (solid symbols) are also shown for comparison. The dopants in PbTe are shown in brackets. For the *Pnma* phase, the highest ZT values are along the *x* and *y* axes for *p*- and *n*-type materials, respectively.

out of 6*s* and 6*p* states of Pb and 5*p* states of Te, while the conduction bands are mainly from 6*p* and 5*p* states of Pb and Te, respectively.

Since transport properties are closely related to the electronic states near the HVB and LCB for the *p*- and *n*-type compounds, respectively, it is reasonable to focus only on the

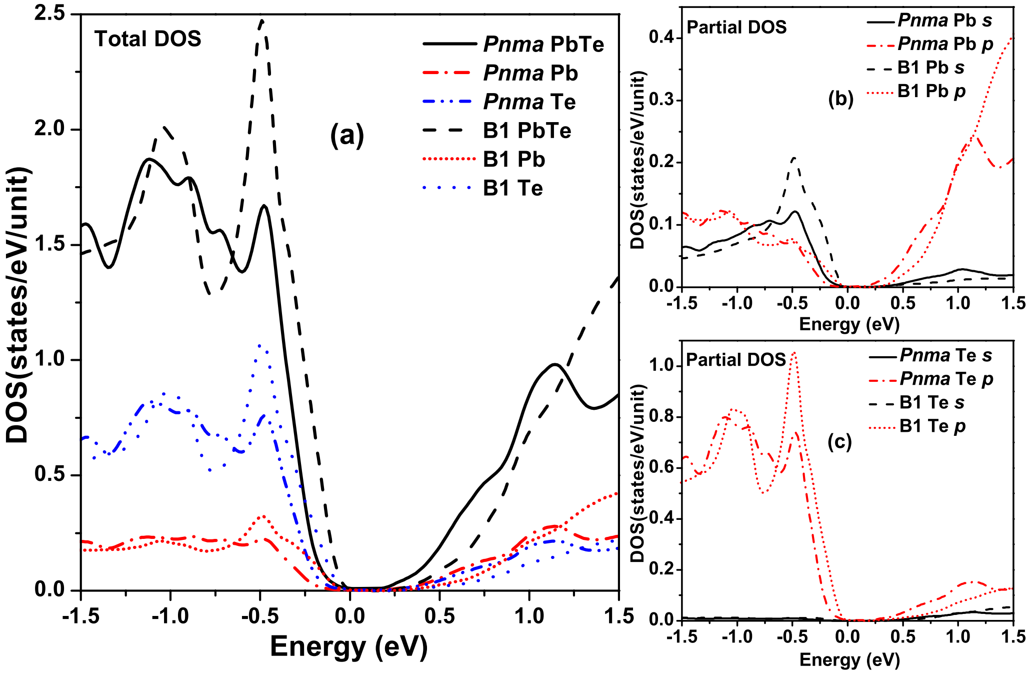

FIG. 5. (Color online) Calculated DOS for PbTe within the B1 and *Pnma* structure at 0 and 6.5 GPa. (a) The total DOS of PbTe, Pb, and Te. (b) Partial DOS of *s* and *p* character for Pb. (c) Partial DOS of *s* and *p* character for Te.

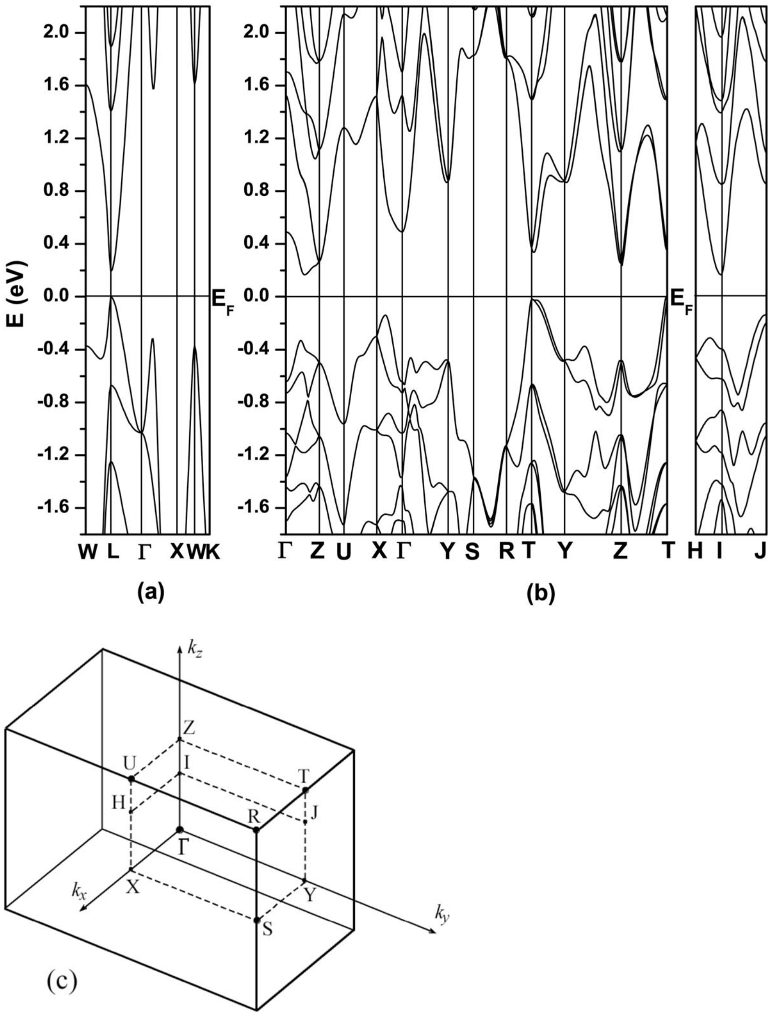

FIG. 6. (a) Band structures of PbTe within the B1 phase at zero pressure. The band gap is shifted to the experimental value of 0.19 eV. (b) Band structures of PbTe within the *Pnma* phase at 6.5 GPa. The band gap is shifted to the value of 0.166 eV provided by EV-GGA. (c) The first BZ of the *Pnma* structure. The principal symmetry points and k points of H (0.5, 0, 0.292), I (0, 0, 0.292), and J (0, 0.5, 0.292) are shown in the first BZ.

energy range near the band gap. It is shown in Fig. 5(a) that the total DOS of the *Pnma* phase is higher than that of the B1 phase near the LCB, in contrast to the fact that the B1 phase has a higher total DOS near the HVB. Therefore, it is suggested that at the phase transition of B1-*Pnma*, there is an enhancement of the DOS near the LCB, whereas a reduced DOS near the HVB. The materials with high S are usually associated with a large DOS near the band gap.[30] So the current DOS results are mainly responsible for the predicted higher and lower S in the *Pnma* structure than those in the B1 phase for n- and p-type materials, respectively, as shown in Figs. 3(a) and 3(b). The analysis of partial DOS indicates that the increased DOS near the LCB is dominated by the p states of Pb and Te, while the decreased DOS near the HVB is from the s and p states of Pb and p states of Te.

Figures 6(a) and 6(b) show the energy band structure along the principal symmetry directions of the B1 and *Pnma* structures at 0 and 6.5 GPa, respectively. Figure 6(c) is a description of the first BZ for the *Pnma* structure. From Fig. 6(a), it can be clearly seen that the maximum of the HVB and the minimum of the LCB for the B1 phase lie at the L point (0.5, 0.5, 0.5), indicating a direct band gap nature. Both LCB and HVB are calculated to be twofold degenerate. From Fig. 6(b) for the *Pnma* phase, the minimum of the LCB lies along the ΓZ direction [k_z direction in Fig. 6(c)] at the I point (0, 0, 0.292), while the maximum of the HVB sits in the ZT direction at the k point (0, 0.49, 0.5), resulting in an indirect band gap. Note that H point (0.5, 0, 0.292) and J point (0, 0.5, 0.292), as shown in Figs. 6(b) and 6(c), were introduced in the band structure plot in order to discuss the energy dispersion near the I point along two other main directions of k_x and k_y in the LCB. The band energy at the k point of (0, 0.49, 0.5) is only 0.019 eV higher than that of the T point (0, 0.5, 0.5) [Fig. 6(c)], thus, for simplicity, we discuss the energy dispersion near the T point in the HVB.

Mahan and Sofo[48] demonstrated that for good thermoelectric materials, the energy distribution of carriers should be narrow and have a high carrier velocity in the direction of the applied field, which is possible in a highly anisotropic system. Here, we can infer some favorable features for good

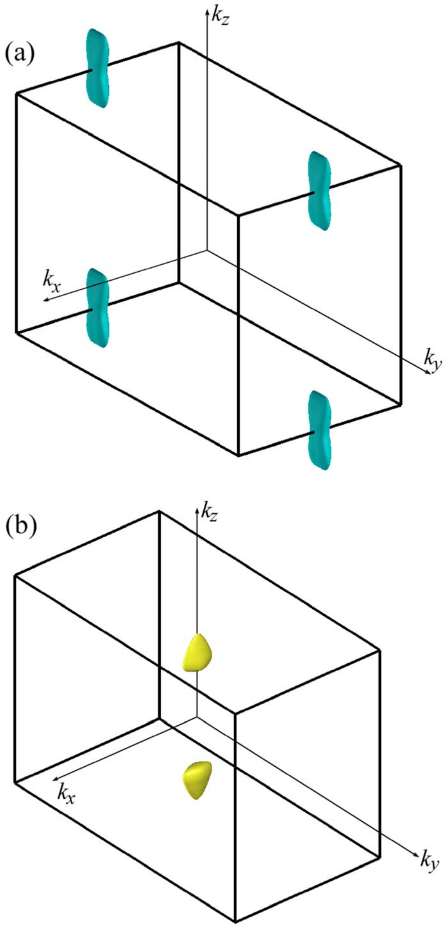

FIG. 7. (Color online) Constant energy surfaces in the first BZ for the *Pnma* phase of PbTe at 6.5 GPa: (a) 0.05 eV below the maximum of HVB. Four energy pockets are shown, and each side along k_x in the first BZ own a quarter of a pocket. (b) 0.05 eV above the minimum of LCB.

anisotropic thermoelectric materials from the curve of $(\varepsilon\text{-}\mu)\partial f/\partial\varepsilon$ that enters the expression for the S as shown in Fig. 1. At 300 K, the extrema of the $(\varepsilon\text{-}\mu)\partial f/\partial\varepsilon$ function are located approximately at $|\varepsilon\text{-}\mu|=0.05$ eV, and the optimal carrier concentration will therefore correspond to a chemical potential close to the band edges.[17] The constant energy surface within 0.05 eV near the band edge should have a large area to increase the DOS and S, while a small area along the other direction to increase the group velocity[17] and conductivity [Eqs. (1)–(4)]. One example of this kind of constant energy surface is a flat pocket of p-type CsBi_4Te_6.[17] Both the large and small areas along different directions on the same constant energy surface lead to a large power factor $S^2\sigma$.

From Fig. 6(b) for the *Pnma*, it is found that the largest band dispersions near the k points of T and I in the HVB and LCB, respectively, are along the TR (k_x) and IJ (k_y) directions. Since the group velocity can be expressed by Eq. (3), it is suggested that the largest group velocities are along the directions of k_x in the HVB and k_y in the LCB in the reciprocal space. Figure 7 shows the constant energy surface within 0.05 eV below and above the extrema of HVB and LCB edges for the *Pnma* phase. It is clear that the large dispersion along the TR and IJ directions in Fig. 6(b) results in the small areas on the constant energy surface along k_x in the HVB and k_y in the LCB for the p- and n-type compounds, respectively, as shown in Figs. 7(a) and 7(b). It is noted that there also exist large areas along other directions. The coexistence of large and small areas on the same constant energy surface in the *Pnma* phase results in large Seebeck coefficients and conductivities for both of the p- and n-type samples at 6.5 GPa. The above analyses indicate that the strong anisotropy for the *Pnma* phase in the electronic structure is mainly responsible for the high thermoelectric performance.

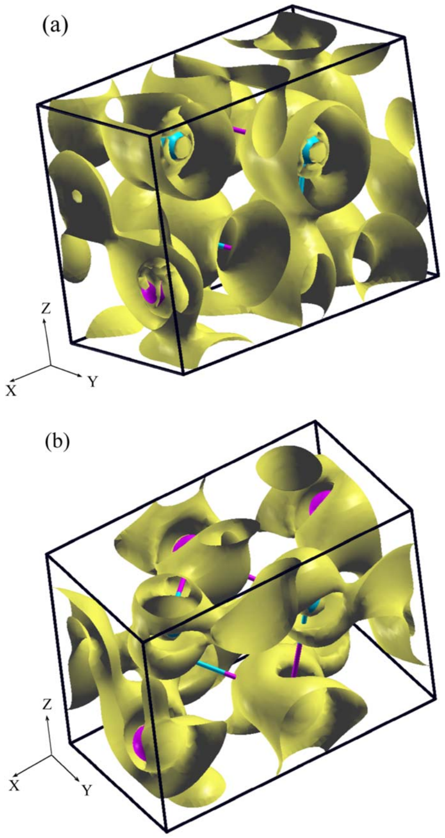

FIG. 8. (Color online) Constant electron density surface plot for the *Pnma* phase of PbTe at 6.5 GPa: (a) energy range at 0.1 eV below the maximum of HVB. The surface covers a volume where the electron density is larger than 2×10^{-5} e/$\AA^3$. (b) Energy range at 0.1 eV above the minimum of LCB. The surface covers a volume where the electron density is larger than 5×10^{-5}e/$\AA^3$. The pink spheres represent Pb, and the light blue spheres represent Te.

Why is the energy distribution so anisotropic for the *Pnma* phase? The answer could be found in the constant electron density surface within the energy windows of 0.1 eV below and above the HVB and LCB in Fig. 8. The choice of 0.1 eV is from the fact that the carriers in the energy range of ±0.1 eV contribute mostly to the transport properties at 300 K as indicated in the plot of $(\varepsilon\text{-}\mu)\partial f/\partial\varepsilon$ (Fig. 1). Figure 8(a) shows that the constant electron density is mainly distributed along the y and z axes in direct space, causing a small density change for the HVB along the k_y and k_z directions in the reciprocal BZ. On the contrary, large

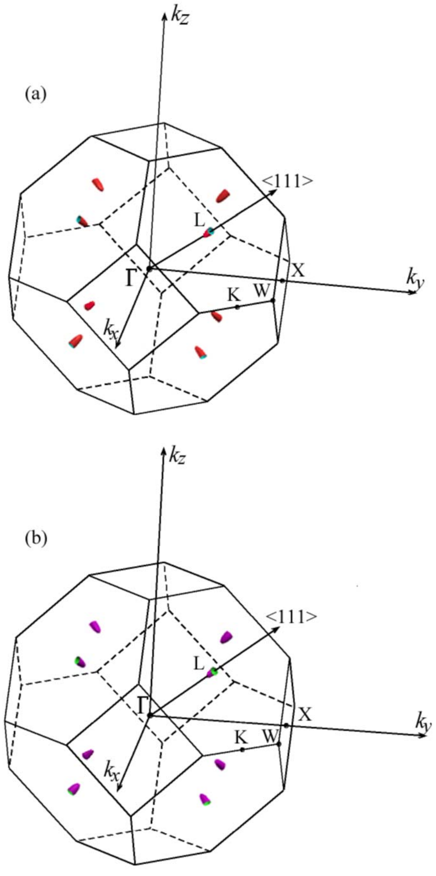

FIG. 9. (Color online) Constant energy surfaces in the first BZ for the B1 phase of PbTe at 0 GPa: (a) 0.05 eV below the maximum of HVB and (b) 0.05 eV above the minimum of LCB. The constant energy surfaces in (a) and (b) are twofold degenerate. The principal symmetry k points and $\langle 111\rangle$ axis are also shown.

density changes are expected along k_x, resulting in a small constant energy surface in this direction. It is noteworthy that the dominant constant electron density for the LCB is mainly located at the x and z directions [Fig. 8(b)], contributing to a large energy dispersion along k_y.

Figures 9(a) and 9(b) show the constant energy surfaces for the B1 structure. It is found that there are eight half-ellipsoid constant energy surfaces along $\langle 111\rangle$. The most striking feature of these half-ellipsoids is the anisotropy of their distributions. For instance, for the pocket along the $\langle 111\rangle$ axes, there is a larger dispersion along the LW direction than that along $L\Gamma$. This anisotropy can also be verified from the band structure plot in Fig. 6(a). It is clear that compared with the $L\Gamma$ direction, there is a larger band dispersion along the LW direction. The obvious anisotropy of the band dispersion causes a large anisotropy for the longitudinal (m_l^*) and transverse (m_t^*) effective masses along $\langle 111\rangle$. It was previously demonstrated that m_l^* is about ten times larger than m_t^*.[49] From the equation of conductivity effective mass (m_c^*) and carrier mobility,[50] it is shown that the large anisotropy in effective masses, and especially the small value of m_t^*, is helpful to get a small m_c^* and a large carrier mobility. Note that each pocket in Fig. 9 is twofold degenerate, so there are 16 half-ellipsoids in the BZ. All of these half-ellipsoids are useful to increase the areas of the constant energy surfaces and the DOS near the band gap, and are responsible for the reasonably large S in the B1 phase.

IV. CONCLUSION

The transport properties and electronic structure of PbTe within the B1 and *Pnma* structures were extensively studied by a combination of first-principles electronic structure calculations and the semiclassical Boltzmann theory. We found that it is important to use the correct band gap to calculate the transport coefficient, especially in the low carrier concentration. The calculated n-type S in the B1 phase is in good agreement with the experimental value, but an obvious overestimation for the p-type one originated from the assumption of the constant relaxation time. The ZT values of the n-type *Pnma* phase at 6.5 GPa are calculated to be about two times larger than that of the n-type B1 phase at ambient pressure. The high thermoelectric performance of the *Pnma* phase at 6.5 GPa is due to its highly anisotropic electronic structure, resulting in the anisotropic energy distribution and large DOS in the conduction band.

Since the *Pnma* phase of PbTe possesses a very high thermoelectric performance, it is desirable to synthesize this phase at ambient condition for utilization. Previously, Baleva *et al.*[51,52] reported the successfully synthesized thin films of another orthorhombic phase and B2 phases of PbTe at ambient pressure. The synthesized method of changing the rate of supercooling could be regarded as a good choice to pursue the *Pnma* phase at ambient condition. Also, high-pressure and high-temperature synthesis could be an alternative method. Besides, for the well-known "diamond" example, Saito *et al.*[53] successfully obtained the single crystal of the high-pressure phase of $(VO)_2P_2O_7$ by slowly cooling the melt at 3 GPa. By all appearances, further experimental exploration is needed to fully make use of the high thermoelectric performance of *Pnma* PbTe.

ACKNOWLEDGMENTS

The authors gratefully acknowledge the financial support of the NSAF of China (No. 10676011), the China 973 Program (No. 2005CB724400), the NBRPP of China (No. 2001CB711201), the NDFCEM (No. 20050183062), the SRF for ROCS, SEM, the Key Research Program of the Education Ministry of China (Grant No. 03057), the National Natural Science Foundation of China (Grant No. 50171030), the Program for 2005 New Century Excellent Talents in University, and the 2006 Project for Scientific and Technical Development of Jilin Province.

[*] Author to whom correspondence should be addressed. mym@jlu.edu.cn

[1] C. Wood, Rep. Prog. Phys. **51**, 459 (1988).

[2] E. A. Skrabek and D. S. Trimmer, in *CRC Handbook of Thermoelectrics*, edited by D. M. Rowe (CRC, Boca Raton, FL, 1995), p. 267.

[3] K. F. Hsu, S. Loo, F. Guo, W. Chen, J. S. Dyck, C. Uher, T. Hogan, E. K. Polychroniadis, and M. G. Kanatzidis, Science **303**, 818 (2004).

[4] E. Quarez, K. F. Hsu, R. Pcionek, N. Frangis, E. K. Polychroniadis, and M. G. Kanatzidis, J. Am. Chem. Soc. **127**, 9181 (2005).

[5] T. C. Harman, D. L. Sprears, and M. J. Manfra, J. Electron. Mater. **25**, 1121 (1996).

[6] T. C. Harman, P. J. Taylor, M. P. Walsh, and B. E. LaForge, Science **297**, 2229 (2002).

[7] N. M. Ravindra and V. K. Srivastava, Phys. Status Solidi A **58**, 311 (1980).

[8] V. V. Shchennikov, S. V. Ovsyannikov, and A. Y. Derevskov, Phys. Solid State **44**, 1845 (2002).

[9] T. Chattopadhyay, H. G. von Schnering, W. A. Grosshans, and W. B. Holzapfel, Physica B & C **139/140**, 356 (1986).

[10] G. Rousse, S. Klotz, A. M. Saitta, J. Rodriguez-Carvajal, M. I. McMahon, B. Couzinet, and M. Mezouar, Phys. Rev. B **71**, 224116 (2005).

[11] S. V. Ovsyannikov and V. V. Shchennikov, Appl. Phys. Lett. **90**, 122103 (2007).

[12] D. Singh, *Planewaves, Pseudopotentials, and the LAPW Method* (Kluwer Academic, Boston, 1994).

[13] P. Hohenberg and W. Kohn, Phys. Rev. **136**, B864 (1964); W. Kohn and L. Sham, Phys. Rev. **140**, A1133 (1965).

[14] P. Blaha, K. Schwarz, G. K. H. Madsen, D. Kvasnicka, and J. Luitz, *WIEN2k, An Augmented Plane Wave Plus Local Orbitals Program for Calculating Crystal Properties.* (Vienna University of Technology, Austria, 2001).

[15] J. P. Perdew, K. Burke, and M. Ernzerhof, Phys. Rev. Lett. **77**, 3865 (1996).

[16] E. Engel and S. H. Vosko, Phys. Rev. B **47**, 13164 (1993).

[17] L. Lykke, Bo B. Iversen, and G. K. H. Madsen, Phys. Rev. B **73**, 195121 (2006).

[18] P. B. Allen, in *Quantum Theory of Real Materials*, edited by J. R. Chelikowsky and S. G. Louie (Klüwer, Boston, 1996), pp. 219–250.

[19] T. J. Scheidemantel, C. Ambrosch-Draxl, T. Thonhauser, J. V. Badding, and J. O. Sofo, Phys. Rev. B **68**, 125210 (2003).

[20] G. K. H. Madsen, K. Schwarz, P. Blaha, and D. J. Singh, Phys. Rev. B **68**, 125212 (2003).

[21] D. J. Singh and I. I. Mazin, Phys. Rev. B **56**, R1650 (1997).

[22] L. Møllnitz, N. P. Blake, and H. J. Metiu, Chem. Phys. **117**, 1302 (2002).

[23] T. Thonhauser, T. J. Scheidemantel, and J. O. Sofo, Appl. Phys. Lett. **85**, 588 (2004).

[24] L. Bertini and C. Gatti, J. Chem. Phys. **121**, 8983 (2004).

[25] G. K. H. Madsen, J. Am. Chem. Soc. **128**, 12140 (2006).

[26] W. W. Schulz, P. B. Allen, and N. Trivedi, Phys. Rev. B **45**, 10886 (1992).

[27] G. K. H. Madsen and D. J. Singh, Comput. Phys. Commun. **175**, 67 (2006).

[28] K. Seeger, *Semiconductor Physics, An Introduction* (Springer Verlag, Berlin, 2002), Chaps. 4 and 6.

[29] N. W. Ashcroft and N. D. Mermin, *Solid State Physics* (Saunders, Philadelphia, 1976), Chaps. 13 and 28.

[30] X. Gao, K. Uehara, D. D. Klug, S. Patchkovskii, J. S. Tse, and T. M. Tritt, Phys. Rev. B **72**, 125202 (2005).

[31] T. Thonhauser, T. J. Scheidemantel, J. O. Sofo, J. V. Badding, and G. D. Mahan, Phys. Rev. B **68**, 085201 (2003).

[32] R. Dalven, in *Solid State Physics*, edited by H. Ehrenreich, F. Seitz, and D. Turnbull (Academic, New York, 1973), Vol. 28, p. 179.

[33] M. L. Cohen and J. R. Chelikowsky, in *Electronic Sructure and Optical Properties of Semiconductors*, 2nd ed., edited by M. Cardona, Springer Series in Solid State Sciences Vol. 75 (Springer-Verlag, Berlin, 1989).

[34] O. Gunnarsson and K. Schönhammer, Phys. Rev. Lett. **56**, 1968 (1986).

[35] R. W. Godby, M. Schlüter, and L. J. Sham, Phys. Rev. Lett. **56**, 2415 (1986).

[36] M. S. Hybertsen and S. G. Louie, Phys. Rev. B **34**, 5390 (1986).

[37] A. J. Crocker and L. M. Rogers, Br. J. Appl. Phys. **18**, 563 (1967).

[38] Y. Noda, M. Orihashi, and I. A. Nishida, Mater. Trans., JIM **39**, 602 (1998).

[39] M. Orihashi, Y. Noda, H. T. Kaibe, and I. A. Nishida, Mater. Trans., JIM **39**, 672 (1998).

[40] P. Zhu, Y. Imai1, Y. Isoda1, Y. Shinohara, X. Jia, and G. Zou, Mater. Trans. **46**, 761 (2005).

[41] P. Zhu, Y. Imai, Y. Isoda, Y. Shinohara, X. Jia, and G. Zou, J. Phys.: Condens. Matter **17**, 7319 (2005).

[42] E. A. Gurieva, P. P. Konstantinov, L. V. Prokof'eva, Yu. I. Ravich, and M. I. Fedorov, Semiconductors **37**, 276 (2003).

[43] L. M. Rogers, Br. J. Appl. Phys. **18**, 1227 (1967).

[44] D. M. Freik, L. I. Nykyruy, and V. M. Shperun, Semicond. Phys., Quantum Electron. Optoelectron. **5**, 362 (2002).

[45] H. J. Goldsmid, *Electronic Refrigeration* (Pion, London, 1986), p. 10.

[46] D. M. Rowe and C. M. Bhandari, *Modern Thermoelectrics* (Reston, Reston, VA, 1983), p. 104.

[47] L. D. Hicks and M. S. Dresselhaus, Phys. Rev. B **47**, 12727 (1993).

[48] G. D. Mahan and J. O. Sofo, Proc. Natl. Acad. Sci. U.S.A. **93**, 7436 (1996).

[49] G. Martinez, M. Schlüter, and Marvin L. Cohen, Phys. Rev. B **11**, 651 (1975).

[50] H. A. Lyden, Phys. Rev. **135**, A514 (1964).

[51] M. Baleva and E. Mateeva, Phys. Rev. B **50**, 8893 (1994).

[52] M. Baleva, L. Bozukov, and M. Momtchilova, J. Phys.: Condens. Matter **4**, 4633 (1992).

[53] T. Saito, T. Terashima, M. Azuma, M. Takano, T. Goto, H. Ohta, W. Utsumi, P. Bordet, and D. C. Johnston, J. Solid State Chem. **153**, 124 (2000).